A PARAMETERIZATION STUDY FOR ACOUSTIC FULL WAVEFORM INVERSION

A. Przebindowska, A. Kurzmann, D. Köhn, T. Bohlen

email: *anna.przebindowska@kit.edu*

keywords: *waveform tomography, multi-parameter inversion, marine seismics*

ABSTRACT

The aim of this study is to find the most suitable parameterization for the multi-parameter acoustic inversion of marine reflection seismics. We investigate three different combinations of parameters: P-wave velocity and density, P-wave impedance and density, P-wave velocity and P-wave impedance. First we analyze the coupling between parameter pairs to determine how strong the trade-off between parameters is. Since coupling is a function of the offset, we consider separately the near-offset and the full-offset data. We use the acoustic Marmousi model with a conventional streamer geometry, and a frequency range from 3 to 20 Hz. A set of inversion tests is performed to assess the different parameterizations in terms of the quality of the reconstructed images and the convergence rate of the inversion.

We have observed that the coupling between parameters, and thereby the ambiguity of the inversion, is decreasing once the information from far-offsets is included. Our results show, that the choice of the model parameterization mainly affects the reconstruction of the density structures, whereas the resolution of the velocity and impedance models is comparable. The parameter set P-wave velocity and density provided the best convergence rate and the best quality of the reconstructed images.

INTRODUCTION

The aim of the full waveform inversion (FWI) is to estimate the physical properties of the Earth by minimizing the misfit between observed and predicted seismic data. To reconstruct reliable models of the subsurface structures from field measurements, the waveform inversion should correctly account for the most significant wave propagation phenomena present in the data. However, numerous approximations are usually made to limit the number of physical parameters and to reduce the computational cost of the method. For instance, it is common practice to use the acoustic approximation when inverting marine seismic data. In most marine field data applications the authors only invert for the P-wave velocity (Shipp and Singh, 2002; Operto et al., 2004; Boonyasiriwat et al., 2010; Kelly et al., 2010; Delescluse et al., 2011). This mono-parameter acoustic waveform inversion is not correctly describing the amplitudes of field data. In order to improve the accuracy of seismic amplitude modeling, an extension from the mono-parameter inversion to the multi-parameter inversion is a straightforward solution. However, the joint reconstruction of more parameters is more expensive and increase the ill-posedness of the inverse problem (Virieux and Operto, 2009).

In the context of the multi-parameter inversion, an important factor is the choice of the parameters describing the medium (Tarantola, 1986). The acoustic medium can be described by P-wave velocity V_P and density ρ, or the acoustic impedance I_P. Thus the possible parameterizations sets are: P-wave velocity and density, acoustic impedance and density, P-wave velocity and acoustic impedance. The choice of the acoustic parameters may influence the convergence rate and the ambiguity of the inverse problem, and affect the final results (Kolb and Canadas, 1986).

The choice of an adequate parameterization has been mainly investigated for an elastic medium (Tarantola, 1986; Assous and Collino, 1990; Debski and Tarantola, 1995; Köhn et al., 2012). Tarantola (1986) has shown that the model parameters should be related to the parameters of the Earth that can be resolved by a certain acquisition. The typical seismic reflection data contain two different kinds of information: on the long-wavelength seismic wave velocities, and on the short-wavelength impedances (Jannane et al., 1989). For the long wavelengths ($\lambda \geq 300$ m), the misfit function mainly depends on traveltimes of the main reflections, and thus the velocity of the medium. Whereas, for the short wavelengths ($\lambda \leq 60$ m), the data misfit is mainly sensitive to impedance constrasts (the reflection amplitudes). So, the arrival time of the waves provides the information on the velocity distribution and the amplitude information allows to resolve the high-resolution impedance contrasts. Tarantola (1986) suggests that for long wavelenths the P-wave and S-wave velocities are the most adequate parameters and for short wavelengths the seismic impedances and density are more suitable.

Another important aspect is the coupling between different parameters. It would be favorable to select parameters that are as uncorrelated as possible. The trade-off is often investigated by considering the energy radiation patterns of a point diffractor (Tarantola, 1986; Assous and Collino, 1990; Virieux and Operto, 2009). In this case a homogeneous Earth is assumed and each parameter is individually perturbed. Acoustic radiation patterns for different parameter sets are studied in Virieux and Operto. An important observation is that the coupling is a function of the offset. For example, using P-waves only and small offsets it is difficult to distinguish between a density diffractor and a P-wave velocity diffractor. On the other hand, the V_P and I_P point diffractors scatter energy for different apertures, V_P for wide apertures and I_P for short apertures, which might suggest that this is the most adequate parameter set. For instance, this parameterization has been chosen to define the medium in the acoustic multi-parameter inversion of sesimic reflection data performed by Kolb and Canadas (1986).

In this study we test three different acoustic parameterizations. The first parameter set is the P-wave velocity and density $\mathbf{m_1} = [V_P, \rho]$, the second is the P-wave impedance and density $\mathbf{m_2} = [I_P, \rho]$, and the third parameter set is the P-wave velocity and P-wave impedance $\mathbf{m_3} = [V_P, I_P]$. First, we investigate the coupling between the different parameters, when the simultaneous multi-parameter inversion is performed. If there is a strong trade-off between two parameters, this may result in an incorrect solution and may lead to a wrong interpretation of the inversion results. Furthermore, the coupling effects for the same parameter set may vary depending on the maximum offset of the seismic data used in the inversion. For that reason, we investigate separately the multi-parameter inversion of near-offset and full-offset data.

In the second set of experiments, we perform the acoustic waveform inversion of marine reflection seismic data simulated for realistic P-wave velocity and density models. Here, we assess the different model parameterizations in terms of the quality of the reconstructed models and of the convergence rate of the inversion.

THEORETICAL BACKGROUND

Within the full waveform inversion scheme, the model parameters $\mathbf{m}$ are updated iteratively along the conjugate gradient direction $\delta\mathbf{c}$, using the Polak-Ribiere algorithm (Nocedal and Wright, 1999), with the step length μ:

$$\mathbf{m}_{n+1} = \mathbf{m}_n - \mu_n P \delta\mathbf{c}_n \tag{1}$$

where $\mathbf{m}_{n+1}$ is the updated model, and P a preconditioning operator.

The gradient for bulk modulus K and density ρ at iteration n can be written as (Tarantola, 1984):

$$\begin{aligned} \delta K_n &= \frac{1}{K_n^2} \sum_{\text{shots}} \int_t dt \; \frac{\partial p_n}{\partial t} \; \frac{\partial p_n^{'}}{\partial t} \; , \\ \delta \rho_n &= \frac{1}{\rho_n^2} \sum_{\text{shots}} \int_t dt \; \nabla p_n \cdot \nabla p_n^{'} \; , \end{aligned} \tag{2}$$

where $p_n(x, z, t)$ is the forward propagated field in the current model, and $p_n^{'}(x, z, t)$ is generated by propagating the residual data from all receiver positions backward in time.

The gradient expression in terms of new model parameters $\mathbf{m}_{\text{new}}$ can be derived as follows (Mora, 1987):

$$\delta\mathbf{m}_{\text{new}} = \frac{\partial\mathbf{m}}{\partial\mathbf{m}_{\text{new}}}\delta\mathbf{m} \tag{3}$$

It requires the computation of the Jacobian $\partial\mathbf{m}/\partial\mathbf{m}_{\text{new}}$ and the gradient of the original model parameters.

To evaluate the gradient in terms of P-wave velocity and density, we need the relationship between the P-wave velocity V_P, the bulk modulus K and density ρ, which is $K = \rho V_P^2$. The gradient for the P-wave velocity can be expressed as:

$$\delta V_P = \frac{\partial K}{\partial V_P}\,\delta K + \frac{\partial \rho}{\partial V_P}\,\delta\rho = 2\rho V_P\,\delta K\ . \tag{4}$$

The gradient for the density $\delta\rho_{v_p}$ for the parameterization $\mathbf{m_1} = [V_P, \rho]$ can be written as:

$$\delta\rho_{v_p} = \frac{\partial K}{\partial \rho}\,\delta K + \frac{\partial \rho}{\partial \rho}\,\delta\rho = V_P^2\,\delta K + \delta\rho\ . \tag{5}$$

To derive the gradients with respect to the P-wave impedance I_P and density, we use the relationship $K = {I_P}^2/\rho$. The gradients for the parameterization $\mathbf{m_2} = [I_P, \rho]$ are thus:

$$\begin{aligned}\delta I_P &= \frac{2I_P}{\rho}\,\delta K\ ,\\ \delta\rho_{imp} &= -\frac{1}{{I_P}^2}\,\delta K + \delta\rho\ .\end{aligned} \tag{6}$$

Using the equation relating the P-wave impedance I_P and P-wave velocity V_P to the bulk modulus, which is $K = V_P I_P$, the gradients in terms of I_P and V_P can be written as:

$$\begin{aligned}\delta I_P &= \frac{1}{V_P {I_P}^2}\,\delta K\ ,\\ \delta V_{P\,imp} &= \frac{1}{{V_P}^2 I_P}\,\delta K\ .\end{aligned} \tag{7}$$

NUMERICAL EXPERIMENT SETTINGS

Modeling parameters

The numerical tests presented in this study are based on the acoustic Marmousi model (Martin et al., 2006), the P-wave velocity and density models, as well as the resulting P-wave impedance model, are shown in Figure 1. The acquisition geometry mimics the conventional single-component streamer survey. The source is a pressure source, located 7.5 m below the air-water interface, with the Ricker wavelet time function. The frequency content of a signal is limited to a bandwidth from 3 to 20 Hz. The streamer consists of 160 hydrophones with a spacing of 25 m located at 7.5 m depth. The near offset is 100 m and the maximum offset is 4 km. We simulate a moving streamer acquisition with the source points moving from the left to the right part of the model and towing a streamer behind. The total of 50 shot gathers are generated at a 50 m interval with 3 seconds of data. A free surface boundary condition is applied at the top of the model, thus the simulated pressure waveform contains both free surface multiples, as well as the source and receiver ghost.

Inversion settings

To reduce the high complexity of the inverse problem, we use the multi-scale inversion approach proposed by Bunks et al. (1995). The inversion starts at low frequencies and higher frequency content is gradually added. In the time-domain waveform inversion, multiple frequencies are used simultaneously. In order to choose the maximum frequencies of each frequency band, we use the strategy proposed by Sirgue and Pratt (2004), which ensures that the lowest vertical wavenumber at the next frequency is equal to the

highest wavenumber at the current frequency. We apply sequentialy the frequency bands with the following maximum frequencies $f_{\max} = (3, 4, 5.3, 7.1, 9.4; 12.5, 16.6, 20)$ Hz; that define the cutoff frequency for the Butterworth low-pass filter. Furthermore, to correct for the amplitude loss with depth due to geometrical spreading and to enhance deeper parts of the model, the linear gradient scaling with depth is implemented (Mora, 1987). Furthermore, the parameters of the water layer and the source time function are assumed to be known. The starting model of any perturbed parameter is a 1D smooth representation of the true model.

As mentioned above, the coupling is a function of the offset. To investigate this relationship, we perform separately the multi-parameter inversion of the near-offset and of the full-offset data. We define the long-offset data as those data acquired with source-receiver offset greater than the depth to the imaging targets. Our assumed imaging target is a gas lense located at the depth of 1 km. Therefore, the maximum offset of the short-offset data is set to 1.15 km, whereas the full-offset data contains all offsets. Because of the moving streamer acquisition, the far offset is ranging from 1.125 km to the maximum of 4 km. The waves of the long-offset data propagate more horizontally than that of the near-offset data, thus they illuminate the subsurface in a different way. The maximum angle of incidence of a ray reflected at the gas lense is approximately 26° for the short-offset data and 63° in case of the full-offset data.

THE COUPLING EFFECTS

In this section we investigate the trade-off between different parameter sets. This is achieved by performing the multi-parameter inversion for different combinations of parameters $\mathbf{m_1} = [V_P, \rho]$, $\mathbf{m_2} = [I_P, \rho]$, and $\mathbf{m_3} = [V_P, I_P]$. For each configuration, the model parameters are perturbed individually, which results in six combinations of acoustic models. Synthetic data is generated for each set of acoustic models.

Inversion results

The inversion results for the first parameter set $\mathbf{m_1} = [V_P, \rho]$ are shown in Figure 2 for a variable V_P model and constant density, while in Figure 3 V_P is constant and variable density model is used. We can observe a quite strong coupling between V_P and ρ, especially when the near-offset data is inverted. There are velocity structures present in the density models, and strong cross-talk artefacts are visible in the inverted velocity. These artefacts reflect the boundaries of the true density structures (Figure 3). However, the coupling between V_P and ρ, and thereby the ambiguity of the inversion, is significantly decreasing once the information from far-offsets is included. It is clearly visible on the velocity and density profiles (Figure 2d and Figure 3d).

The parameterization with $\mathbf{m_2} = [I_P, \rho]$ is illustrated in Figure 4 and in Figure 5. When considering a perturbation in P-wave impedance with a homogeneous density model, it can be seen that the acoustic impedance model is very well resolved from both near-offset and far-offset data. The final density models contain only weak artefacts resulting from the impedance structures. This indicates that both parameters are not strongly coupled. On the other hand, if we want to consider a perturbation in density only and preserve a zero impedance variation, this will result in unrealistic, negative velocity contrasts. To avoid this unplausible assumption, the true I_P is defined as $I_P = V_{P\,(\text{constant})} \cdot \rho_{(\text{perturbed})}$. The true I_P model is used as a starting model for the inversion. We can observe that the original impedance structures are hardly influenced by the density, both for the near-offset and for the full-offset data (Figure 5d). The density model is fairly well reconstructed, but still the accuracy is not as good as for $\mathbf{m_1} = [V_P, \rho]$. This agrees with the amplitude diffraction pattern analysis shown by Tarantola (1986). A diffractor with a perturbation of density but constant impedances would be hardly visible using surface seismic reflection data with moderate offsets, because it only scatters energy downwards into the medium.

In the third parameterization, the medium is described by the P-wave velocity and the P-wave impedance $\mathbf{m_3} = [V_P, I_P]$. Here, we also face the problem of negative density contrast, which would be introduced if a constant impedance model and a perturbed velocity was assumed. For that reason, we define the true I_P as $I_P = V_{P\,(\text{perturbed})} \cdot \rho_{(\text{constant})}$, which is also an initial model for the inversion (Figure 6a). Relatively strong high-frequency artefacts are present in the inverted velocity model, especially when the near-offset data is inverted. Inversion of the full-offset data improves the quality of the reconstructed V_P model, however at the same time it negatively affects the I_P model (Figure 6d). This means that the trade-off between V_P and I_P is generally increasing while the information from far-offsets is in-

cluded. Furthermore, the estimated optimum step-lengths are very variable and have much higher values than the step-lengths estimated for other parameterizations. This may indicate that the inverse problem is running into a local minimum of the misfit function. Additionally, the velocity and impedance errors are only decreasing up to a certain iteration number, afterwards the model errors are increasing, which is apparently associated with the inversion of the high-frequency data. However, at the same time, the data misfit function is gradually decreasing. Figure 7 shows the FWI results for a perturbed acoustic impedance with a homogeneous velocity model. The impedance structures are fairly well resolved, particularly from the short-offset data. Nevertheless, the velocities contain structural I_P information, which may lead to the incorrect interpretation of the inversion results.

ACOUSTIC MULTI-PARAMETER INVERSION - MARMOUSI2 MODEL

The acoustic data set is generated for the Marmousi model (Figure 1). The near-offset and full-offset data are shown in Figure 1g and 1h respectively. Figure 1d-f represents initial models used in the full waveform inversion. The aim of this experiment is to assess the different model parameterizations in terms of the quality of the reconstructed models and of the convergence rate of the inversion.

The multi-parameter FWI results using the near-offset information are shown in Figure 8. The same data set is inverted using different parameterizations. Additionally, the third parameter, that is not represented by a particular parameter set, is recalculated from the final inverted models. This allows for a comparison of all considered parameter classes. The upper structures of the velocity and impedance models, down to the depth of about 1 km, are well reconstructed. However, the deeper parts of the inverted models show strong high-frequency artefacts. The density is well resolved only in the $\mathbf{m_1} = [V_P, \rho]$ parameterization.

The inversion results of the full-offset data are presented in Figure 9. Here, we can observe that the recovery of all parameters has improved significantly. This suggests, that the far-offset data reduces the ambiguity of the inversion and provides an important information for the reconstruction of the subsurface structures.

The depth profiles intersecting the gas lense are shown in Figure 10. They compare the true model with the inversion results for the near-offset and full-offset data. The resolution of the P-wave velocity and acoustic impedance is comparable for every parameterization. But the main difference concerns the density reconstruction. The density structures are fairly well resolved only in the $\mathbf{m_1} = [V_P, \rho]$ parameterization. The worst density image is obtained, when the $\mathbf{m_2} = [I_P, \rho]$ is used. This poor result has been confirmed by the coupling effects analysis (see Figure 5). On the other hand, the density values recalculated from the inverted velocity and impedance models ($\mathbf{m_3} = [V_P, I_P]$) are significantly underestimated. Some density structures are not reconstructed at all and only the location of density interfaces can be recognized.

Figure 11 illustrates the inversion progress for different parameterizations, when the full-offset data is inverted. The evolution of the data misfit function (Figure 11a) shows the most stable progress and the most effective reduction of the data residuals for parameter set $\mathbf{m_1} = [V_P, \rho]$. The jumps in the misfit function for iterations 1-140 are related to the multi-scale inversion approach. At these iterations the next frequency band is included. The data misfit reduction is much worse for $\mathbf{m_2} = [I_P, \rho]$ and $\mathbf{m_3} = [V_P, I_P]$.

In order to quantitatively assess the inversion results, we measure the model error between the true and reconstructed velocity models. We can observe, that the significant reduction of data residuals is followed by a better reconstruction of the velocity models for $\mathbf{m_1} = [V_P, \rho]$ (Figure 11b) . On the other hand, the convergence of the model error is much slower, when we choose the parameter set $\mathbf{m_2} = [I_P, \rho]$. The worst quality of the final V_P model is provided by the $\mathbf{m_3} = [V_P, I_P]$ parameterization, which can be explained by a poor reconstruction of the density model.

CONCLUSIONS

In this study, we have investigated the influence of different model parameterizations on the multi-parameter acoustic waveform inversion. The numerical experiments have been designed to reflect the field measurement conditions of marine reflection seismics. Since the lack of low frequencies is a general problem in seismic recording, the frequency content of the data is limited to a range from 3 to 20 Hz.

First we analyzed the coupling between different parameters and considered separately the information from the near-offset and far-offset data. The far-offset information used in the inversion reduces the coupling between different parameters, i.e. it reduces the ambiguity of the inversion. When ambiguity is

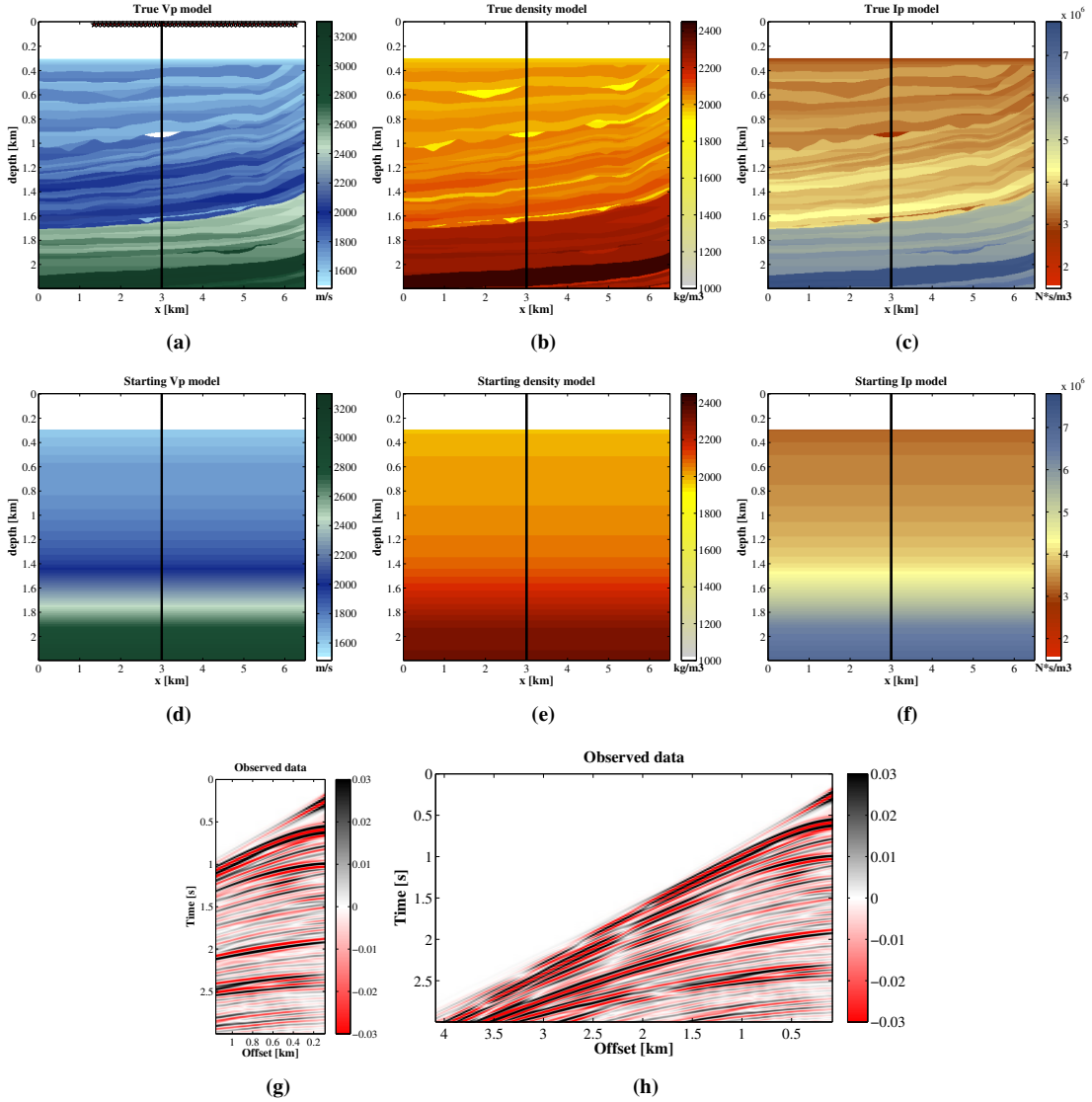

Figure 1: (a) The true P-wave velocity and (b) density models. The stars denote shot point location. (c) The resulting P-wave impedance model $I_P = V_P \rho$. Initial (d) P-wave velocity, (e) density, and (f) impedance models. Acoustic data for true V_P and ρ model, shot 50 located at $x = 6.25$ km: (g) the near-offset data (0.1-1.15 km), (h) the full-offset data (0.1-4.0 km).

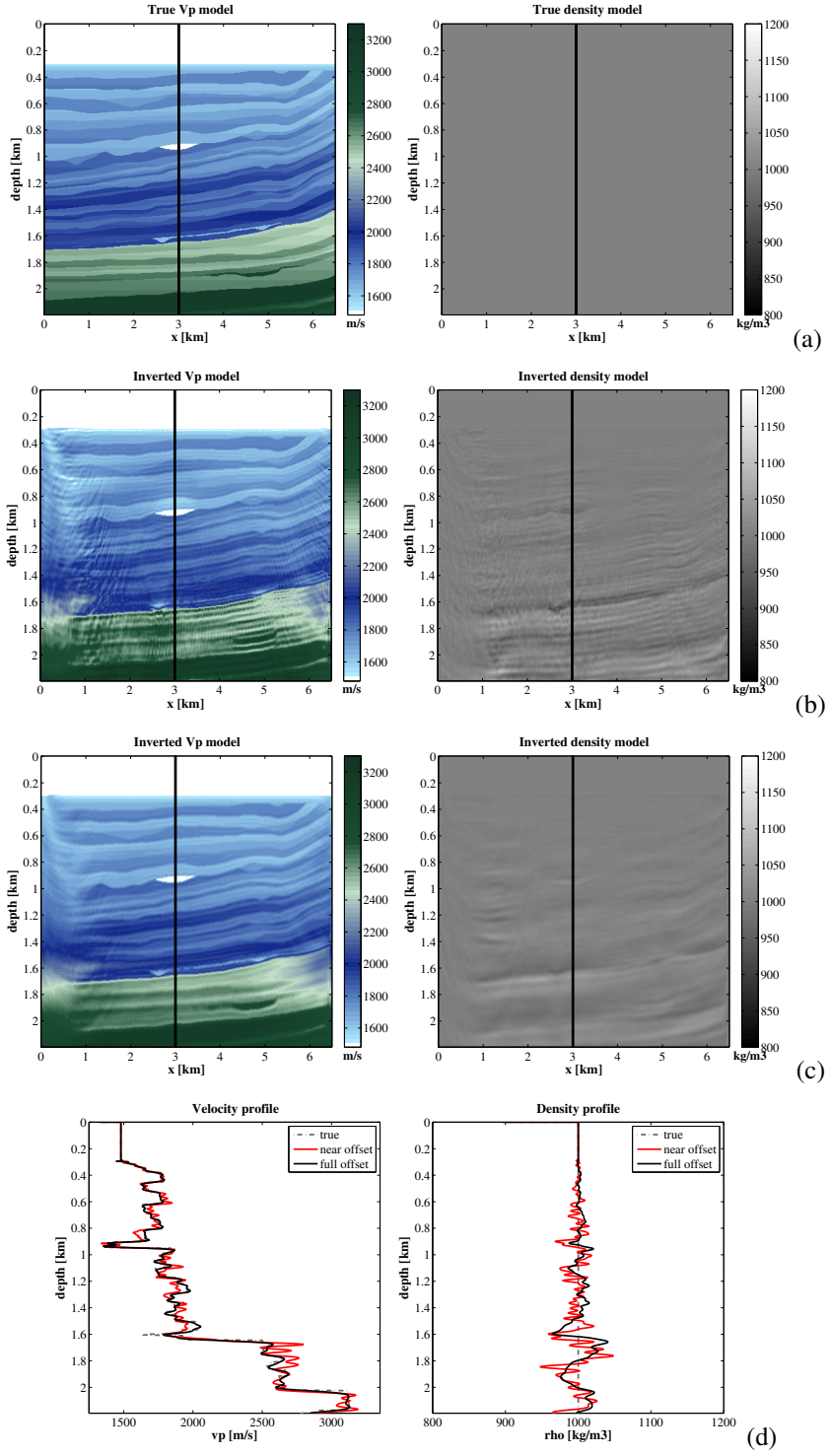

Figure 2: Parameter set $\mathbf{m_1} = [V_P, \rho]$. Perturbation in V_P, homogeneous ρ. (a) True V_P and ρ models; (b) FWI results of the near-offset data (0.1-1.15 km); (c) FWI results of the full-offset data (0.1-4.0 km); (d) V_P and ρ profiles at $x = 3$ km of the true models (dash-dot line) and of the inversion results for the near-offset data (red line) and for the full-offset data (black line).

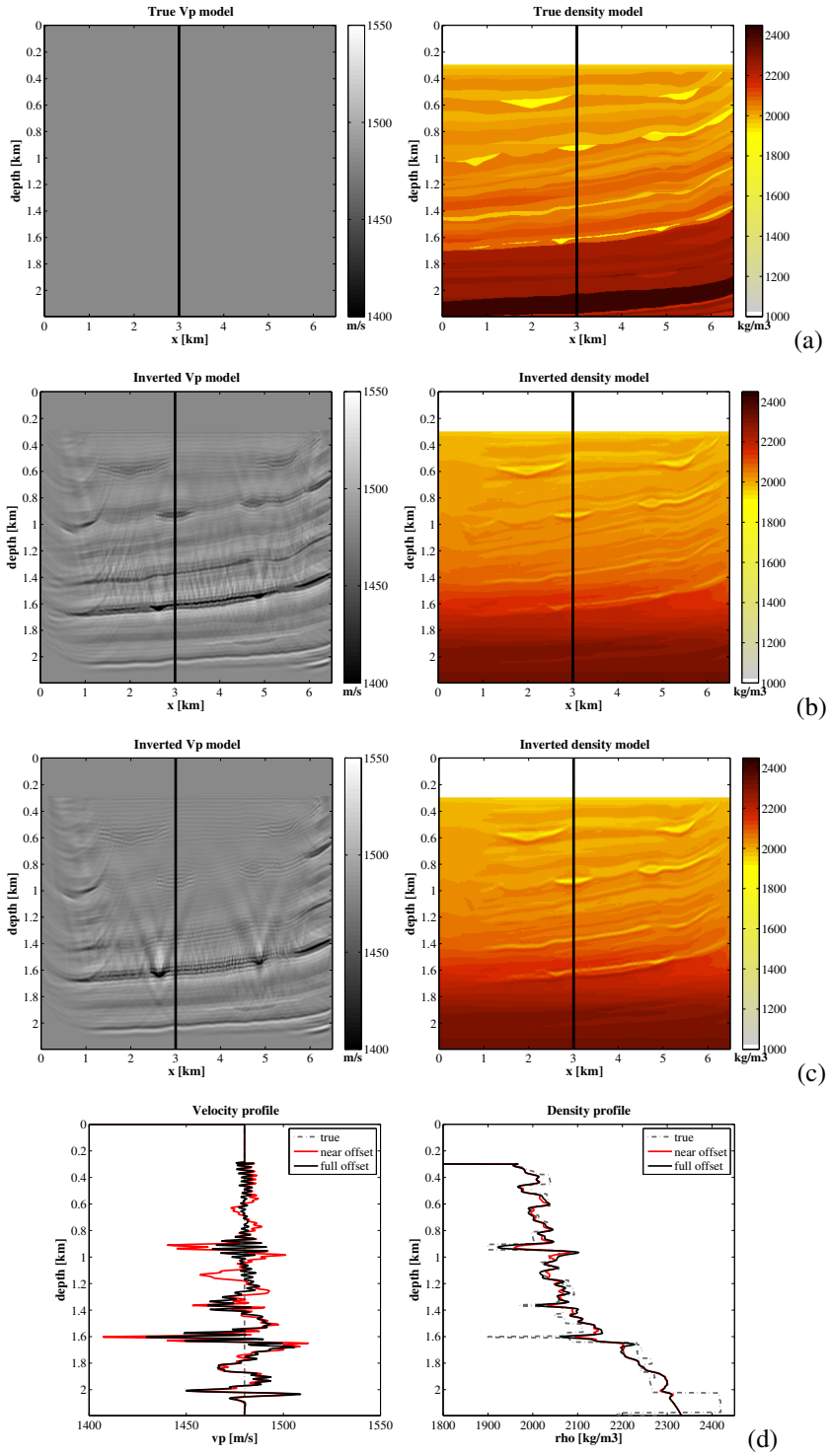

Figure 3: Parameter set $\mathbf{m_1} = [V_P, \rho]$. Perturbation in ρ, homogeneous V_P. (a) True V_P and ρ models; (b) FWI results of the near-offset data (0.1-1.15 km); (c) FWI results of the full-offset data (0.1-4.0 km); (d) V_P and ρ profiles of the true models and of the inversion results.

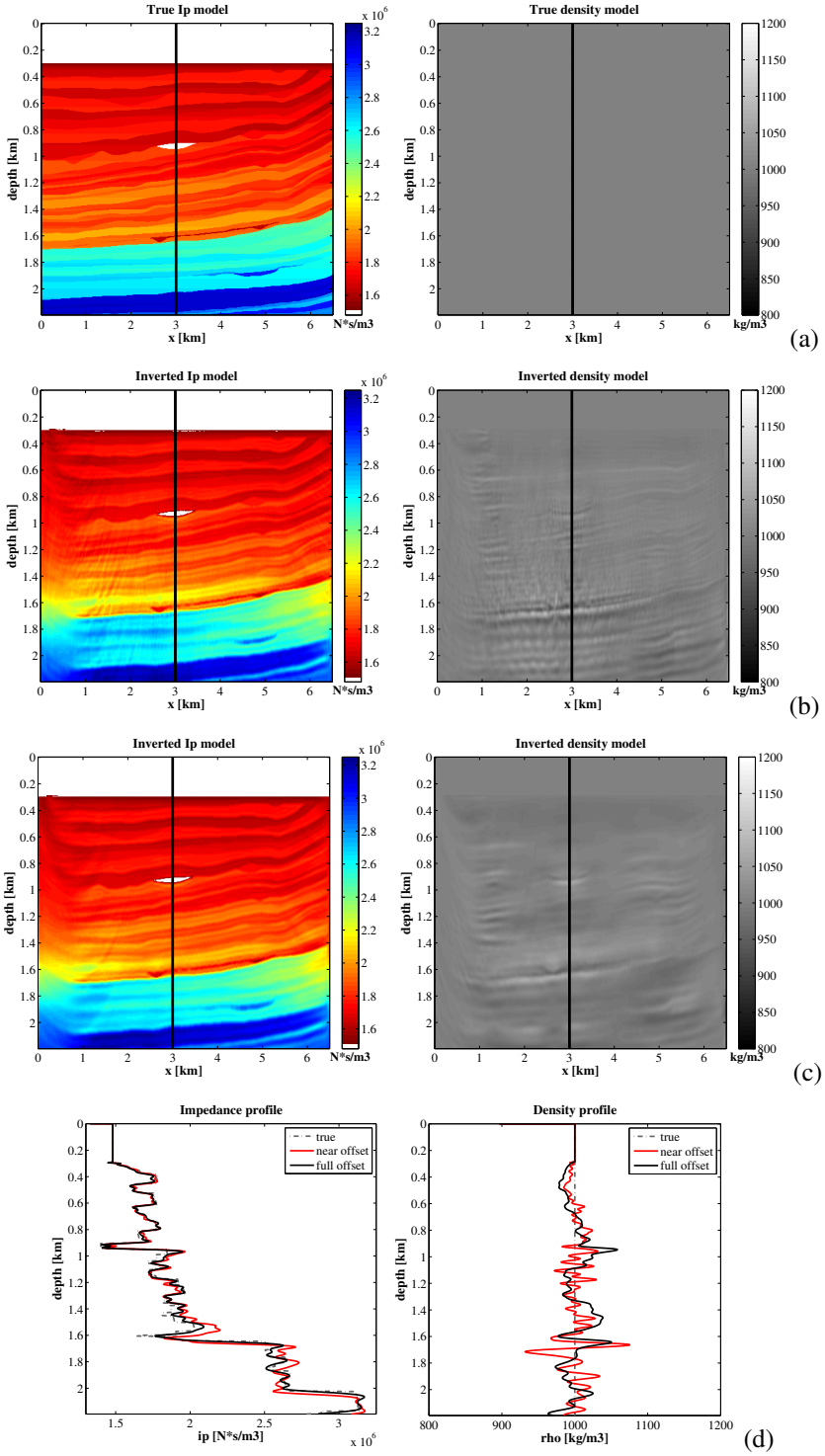

Figure 4: Parameter set $\mathbf{m_2} = [I_P, \rho]$. Perturbation in I_P, homogeneous ρ. (a) True I_P and ρ models; (b) FWI results of the near-offset data (0.1-1.15 km); (c) FWI results of the full-offset data (0.1-4.0 km); (d) I_P and ρ profiles of the true models and of the inversion results.

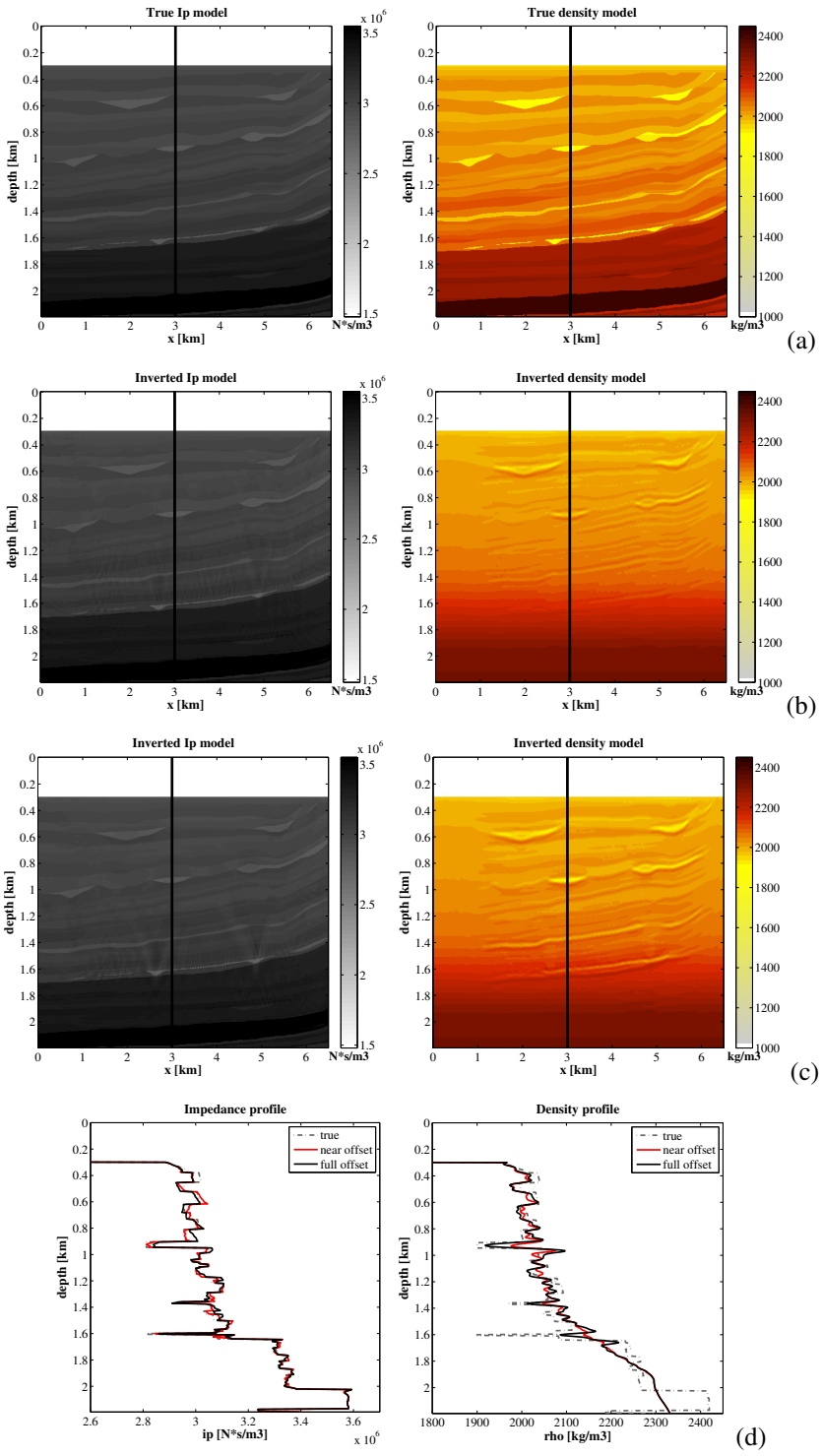

Figure 5: Parameter set $\mathbf{m_2} = [I_P, \rho]$. Perturbation in ρ, $I_P = V_{P(\text{constant})} \cdot \rho_{(\text{perturbed})}$. The true I_P model used as a starting model in the inversion. (a) True I_P and ρ models; (b) FWI results of the near-offset data (0.1-1.15 km); (c) FWI results of the full-offset data (0.1-4.0 km); (d) I_P and ρ profiles of the true models and of the inversion results.

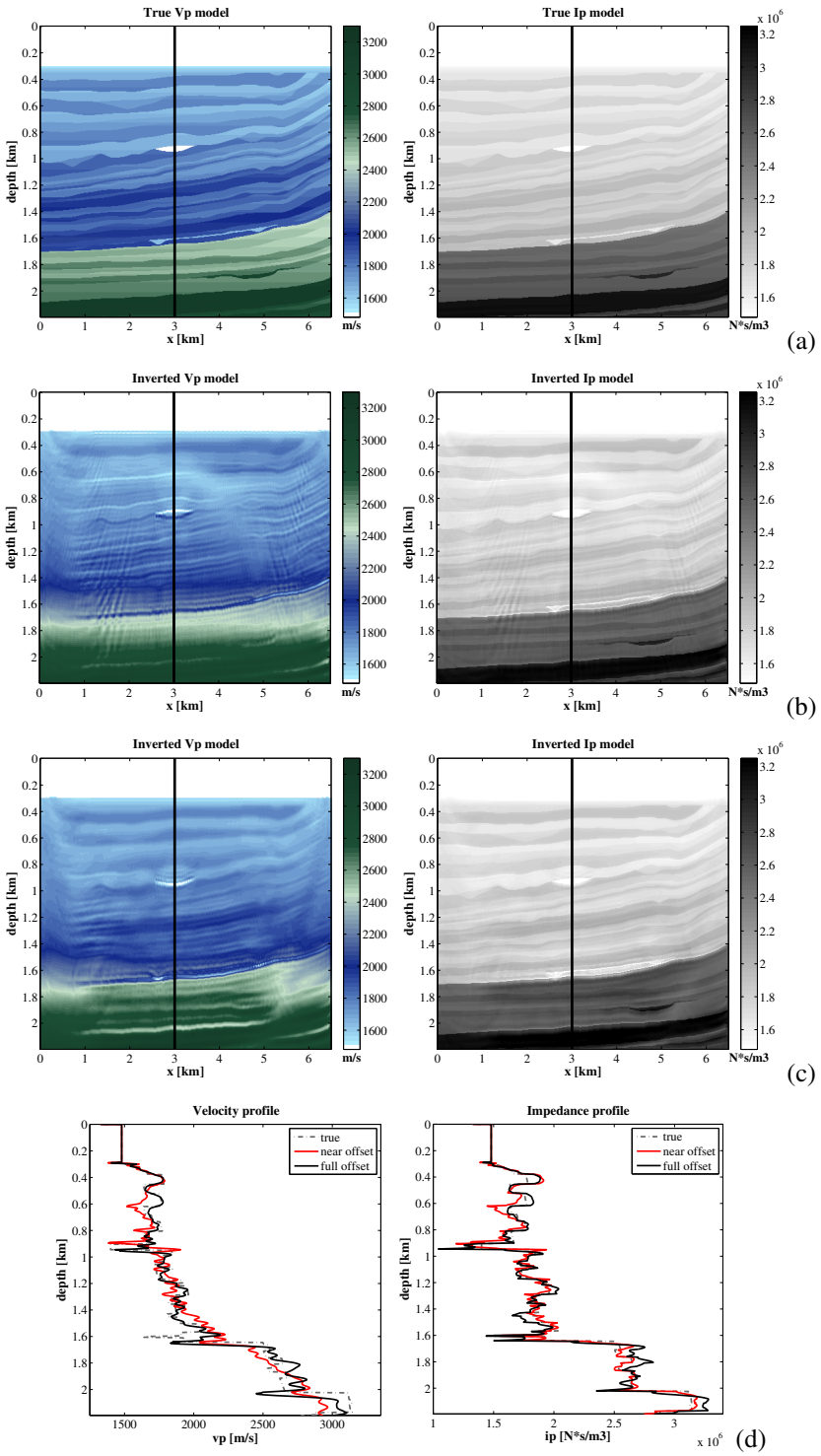

Figure 6: Parameter set $\mathbf{m_3} = [V_P, I_P]$. Perturbation in V_P, $I_P = V_{P\,(\text{perturbed})} \cdot \rho_{(\text{constant})}$. The true I_P model used as a starting model in the inversion. (a) True V_P and I_P models; (b) FWI results of the near-offset data (0.1-1.15 km); (c) FWI results of the full-offset data (0.1-4.0 km); (d) V_P and I_P profiles of the true models and of the inversion results.

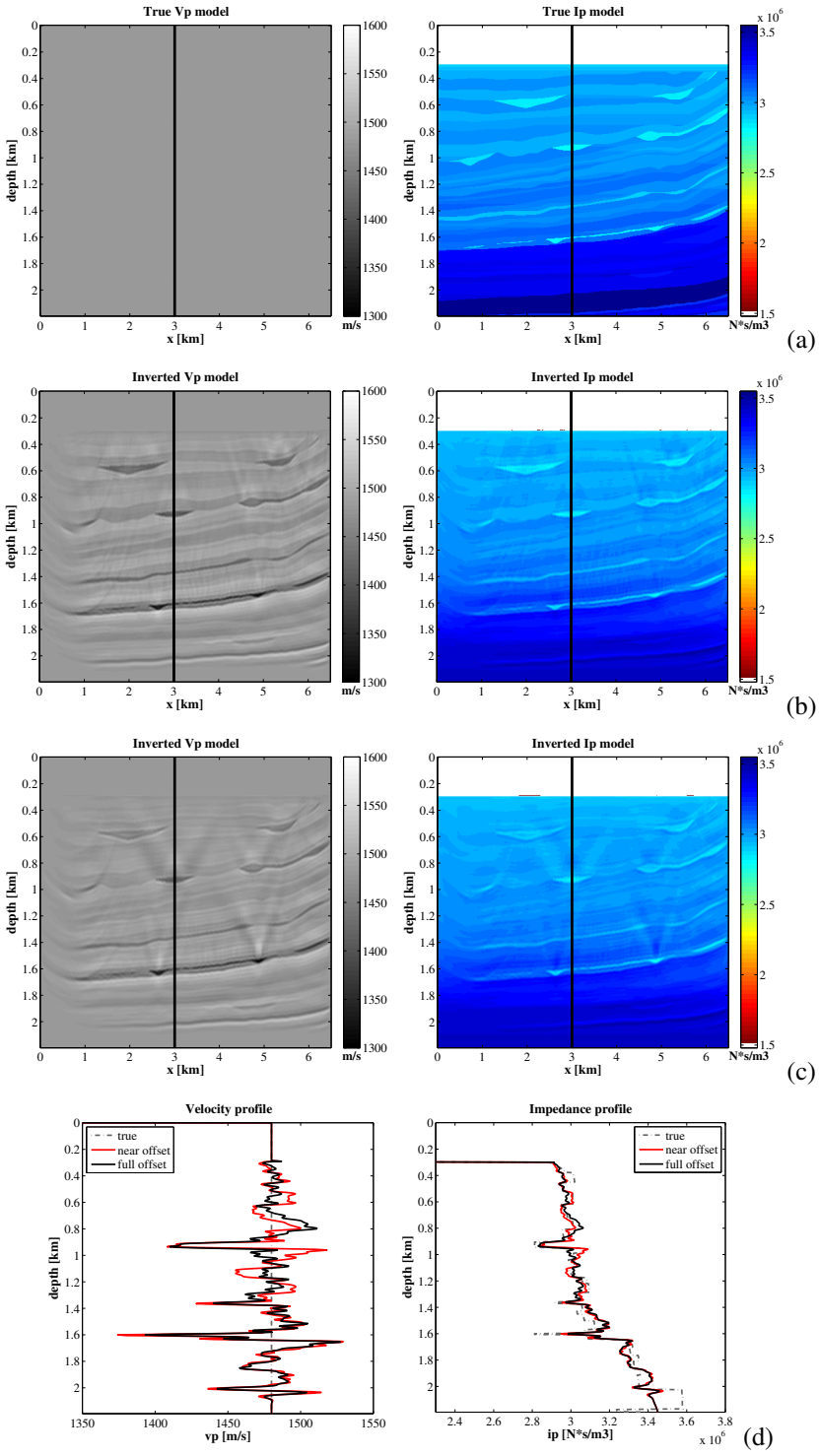

Figure 7: Parameter set $\mathbf{m_3} = [V_P, I_P]$. Perturbation in I_P, homogeneous V_P. (a) True V_P and I_P models; (b) FWI results of the near-offset data (0.1-1.15 km); (c) FWI results of the full-offset data (0.1-4.0 km); (d) V_P and I_P profiles of the true models and of the inversion results.

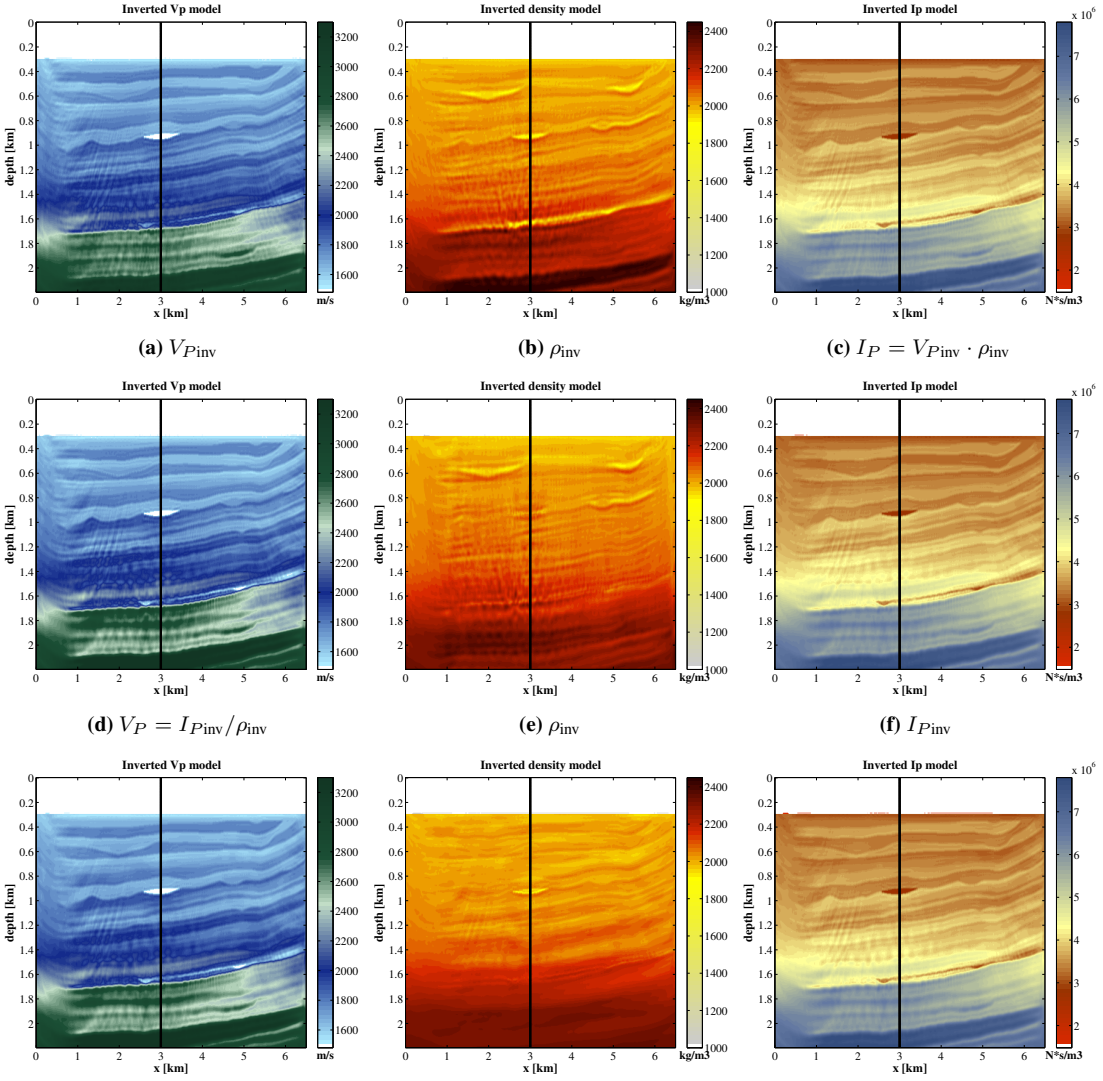

(a) $V_{P\text{inv}}$ **(b)** ρ_{inv} **(c)** $I_P = V_{P\text{inv}} \cdot \rho_{\text{inv}}$

(d) $V_P = I_{P\text{inv}}/\rho_{\text{inv}}$ **(e)** ρ_{inv} **(f)** $I_{P\text{inv}}$

(g) $V_{P\text{inv}}$ **(h)** $\rho = I_{P\text{inv}}/V_{P\text{inv}}$ **(i)** $I_{P\text{inv}}$

Figure 8: Marmousi2 model. FWI results for the near-offset data. Top row $\mathbf{m_1} = [V_P, \rho]$, middle row $\mathbf{m_2} = [I_P, \rho]$, bottom row $\mathbf{m_3} = [V_P, I_P]$. Left: P-wave velocity, middle: density, right: acoustic impedance.

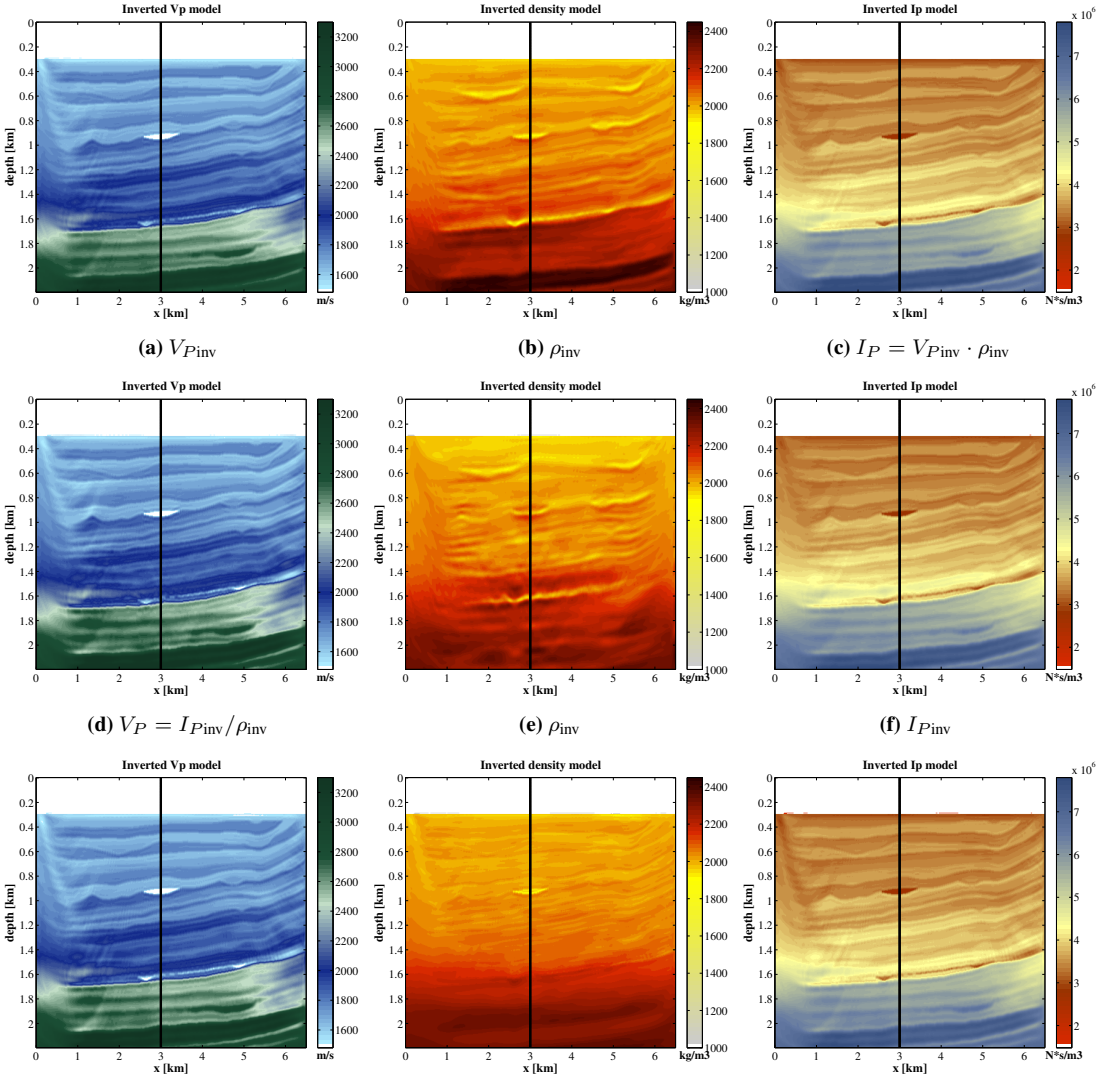

(a) $V_{P\text{inv}}$ **(b)** ρ_{inv} **(c)** $I_P = V_{P\text{inv}} \cdot \rho_{\text{inv}}$

(d) $V_P = I_{P\text{inv}}/\rho_{\text{inv}}$ **(e)** ρ_{inv} **(f)** $I_{P\text{inv}}$

(g) $V_{P\text{inv}}$ **(h)** $\rho = I_{P\text{inv}}/V_{P\text{inv}}$ **(i)** $I_{P\text{inv}}$

Figure 9: Marmousi2 model. FWI results for the full-offset data. Top row $\mathbf{m_1} = [V_P, \rho]$, middle row $\mathbf{m_2} = [I_P, \rho]$, bottom row $\mathbf{m_3} = [V_P, I_P]$. Left: P-wave velocity, middle: density, right: acoustic impedance.

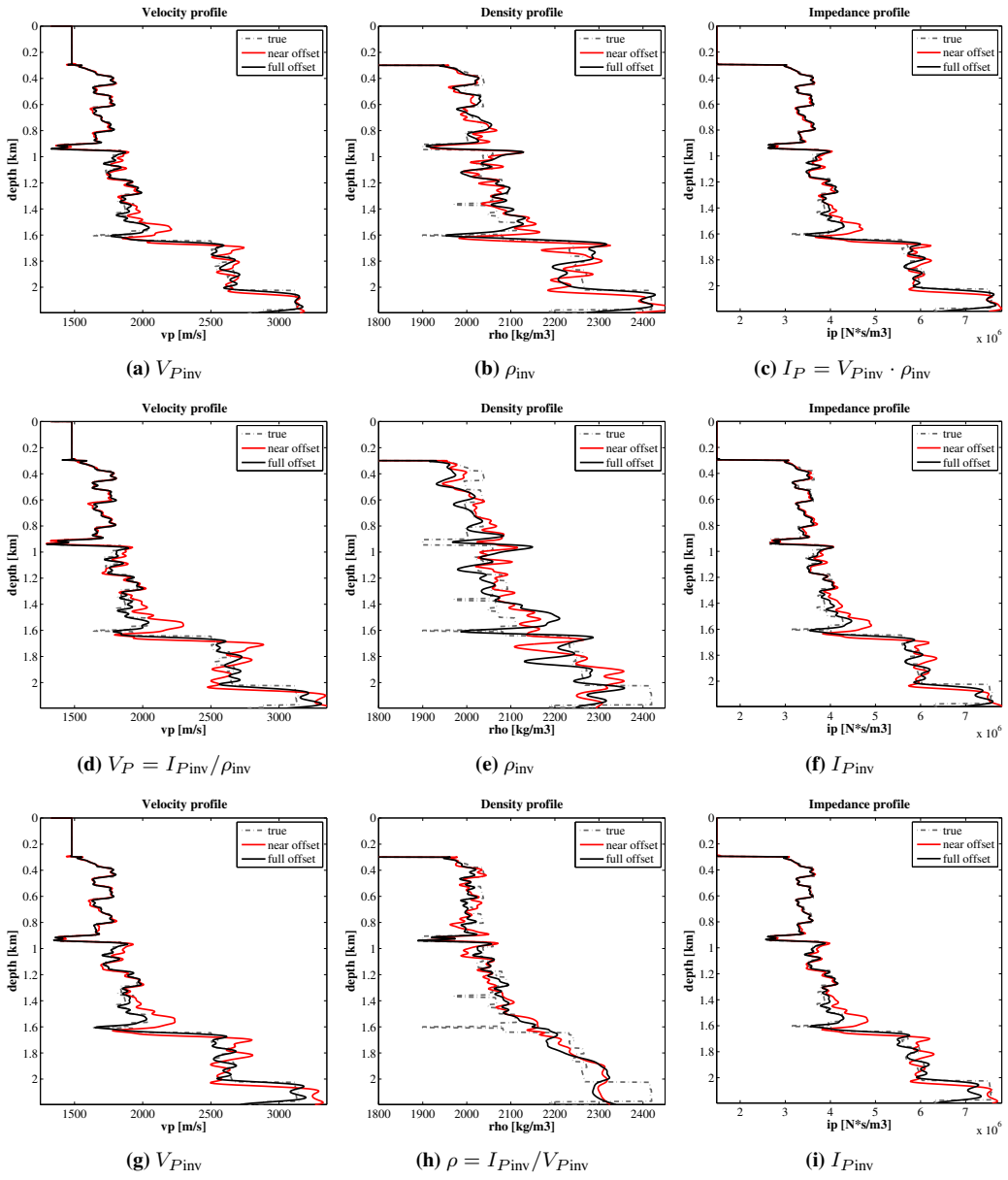

(a) $V_{P\text{inv}}$ **(b)** ρ_{inv} **(c)** $I_P = V_{P\text{inv}} \cdot \rho_{\text{inv}}$

(d) $V_P = I_{P\text{inv}}/\rho_{\text{inv}}$ **(e)** ρ_{inv} **(f)** $I_{P\text{inv}}$

(g) $V_{P\text{inv}}$ **(h)** $\rho = I_{P\text{inv}}/V_{P\text{inv}}$ **(i)** $I_{P\text{inv}}$

Figure 10: Marmousi2 model. Depth profiles at $x = 3$ km of the true models (dash-dot line) and of the FWI results for the near-offset (red solid line) and full-offset data inversion (black solid line). Top row $\mathbf{m_1} = [V_P, \rho]$, middle row $\mathbf{m_2} = [I_P, \rho]$, bottom row $\mathbf{m_3} = [V_P, I_P]$. Left: P-wave velocity, middle: density, right: acoustic impedance.

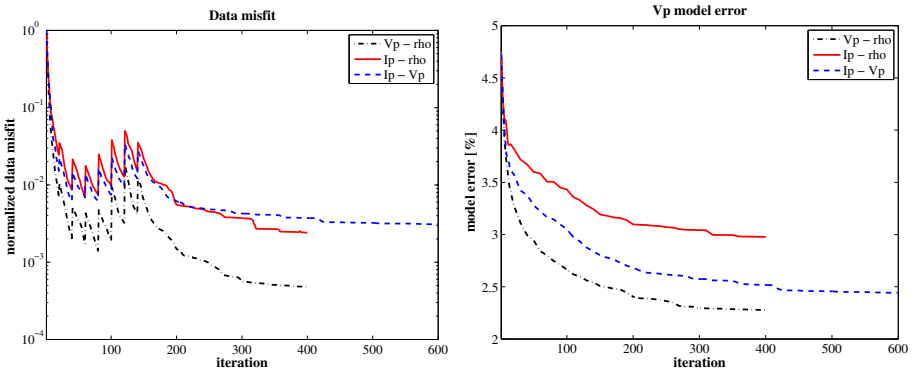

Figure 11: Marmousi2 model. Summary of FWI results for the full-offset data. (a) The evolution of the normalized data misfit function and (b) the V_P model error for different parameterization sets.

present, it results in the incorrect solution and may lead to a wrong interpretation of the inversion results.

The choice of the model parameters is not equivalent for the inversion. Our results show, that the model parameterization mainly affects the reconstruction of the density structures, whereas the resolution of the velocity and impedance models is comparable. Furthermore, it has an influence on the convergence rate and on the stability of the inverse problem. Out of the investigated parameter sets, the velocity and density provided the best convergence rate and the best accuracy of the inverted results.

ACKNOWLEDGMENTS

This work was kindly supported by the sponsors of the *Wave Inversion Technology (WIT) Consortium*, Karlsruhe, Germany. The calculations were performed on the JUROPA cluster at Jülich supercomputing center.

REFERENCES

Assous, F. and Collino, F. (1990). A numerical method for the explanation of sensitivity: the case of the identification of the 2d stratified elastic medium. *Inverse Problems*, 6:487–513.

Boonyasiriwat, C., Schuster, G., Valasek, P., and Cao, W. (2010). Applications of multiscale waveform inversion to marine data using a flooding technique and dynamic early-arrival windows. *Geophysics*, 75(6):R129–R136.

Bunks, C., Saleck, F., Zaleski, S., and Chavent, G. (1995). Multiscale seismic waveform inversion. *Geophysics*, 60(5):1457–1473.

Debski, W. and Tarantola, A. (1995). Information on elastic parameteres obtained from the amplitudes of reflected waves. *Geophysics*, 60(5):1426–1436.

Delescluse, M., Nedimović, M., and Louden, K. (2011). 2d waveform tomography applied to long-streamer mcs data from the scotian slope. *Geophysics*, 76:B151–B163.

Jannane, M., Beydoun, W. B., Crase, E., Cao, D., Koren, Z., Landa, E., Mendes, M., Pica, A., Noble, M., Roeth, G., Singh, S., Snieder, R., Tarantola, A., Trezeguet, D., and Xie, M. (1989). Wavelengths of earth structures that can be resolved from seismic reflection data. *Geophysics*, 54:906–910.

Kelly, S., Ramos-Martinez, J., Tsimelzon, B., and Crawley, S. (2010). Application of an impedance-based full-waveform inversion method for dual-sensor, single-streamer field recordings. *72nd Conference and Technical Exhibition, EAGE, Extended Abstracts*, A020.

Köhn, D., De Nil, D., Kurzmann, A., Przebindowska, A., and Bohlen, T. (2012). On the influence of model parametrization in elastic full waveform tomography. *GJI*, 191:325–345.

Kolb, P. and Canadas, G. (1986). Least-squares inversion of prestack data: Simultaneous identification of density and velocity of stratified media. *SEG Annual Meeting, November 2 - 6, 1986 , Houston, Texas*.

Martin, G., Wiley, R., and Marfurt, K. (2006). Marmousi2 - an elastic upgrade for marmousi. *The Leading Edge*, 25:156–166.

Mora, P. (1987). Nonlinear two-dimensional elastic inversion of multioffset seismic data. *Geophysics*, 52:1211–1228.

Nocedal, J. and Wright, S. (1999). *Numerical optimization*. Springer.

Operto, S., Ravaut, C., Improta, L., Virieux, J., Herrero, A., and Dell'Aversana, P. (2004). Quantitative imaging of complex structures from dense wide-aperture seismic data by multiscale traveltime and waveform inversions: a case study. *Geophysical Prospecting*, 52:625–651.

Shipp, R. and Singh, S. (2002). Two-dimensional full wavefield inversion of wide-aperture marine seismic streamer data. *Geophys. J. Int.*, 151:325–344.

Sirgue, L. and Pratt, R. G. (2004). Efficient waveform inversion and imaging: A strategy for selecting temporal frequencies. *Geophysics*, 69:231–248.

Tarantola, A. (1984). Inversion of seismic reflection data in the acoustic approximation. *Geophysics*, 49:1259–1266.

Tarantola, A. (1986). A strategy for nonlinear elastic inversion of seismic reflection data. *Geophysics*, 51:1893–1903.

Virieux, J. and Operto, S. (2009). An overview of full-waveform inversion in exploration geophysics. *Geophysics*, 74(6):WCC127–WCC152.